

# Demonstration of acousto-optical modulation based on a thin-film AlScN photonic platform

KEWEI BIAN,<sup>1</sup> ZHENYU LI,<sup>1</sup> YUSHUAI LIU,<sup>2,3,4</sup> SUMEI XU,<sup>1</sup> XINGYAN ZHAO,<sup>1</sup>  YANG QIU,<sup>1</sup> YUAN DONG,<sup>1</sup>   
QIZE ZHONG,<sup>1</sup> TAO WU,<sup>2,3,4</sup>  SHAONAN ZHENG,<sup>1,\*</sup> AND TING HU<sup>1,5</sup> 

<sup>1</sup>School of Microelectronics, Shanghai University, Shanghai 201800, China

<sup>2</sup>School of Information Science and Technology, ShanghaiTech University, Shanghai 201210, China

<sup>3</sup>Shanghai Institute of Microsystem and Information Technology, Chinese Academy of Sciences, Shanghai 200050, China

<sup>4</sup>University of Chinese Academy of Sciences, Beijing 100049, China

<sup>5</sup>e-mail: hu-t@shu.edu.cn

\*Corresponding author: snzheng@shu.edu.cn

Received 12 January 2024; revised 15 March 2024; accepted 15 March 2024; posted 15 March 2024 (Doc. ID 517719); published 17 May 2024

Acousto-optic (AO) modulation technology holds significant promise for applications in microwave and optical signal processing. Thin-film scandium-doped aluminum nitride (AlScN), with excellent piezoelectric properties and a wide transparency window, is a promising candidate for achieving on-chip AO modulation with a fabrication process compatible with complementary metal-oxide-semiconductor (CMOS) technology. This study presents, to the best of our knowledge, the first demonstration of AO modulators with surface acoustic wave generation and photonic waveguides monolithically integrated on a 400-nm-thick film of AlScN on an insulator. The intramodal AO modulation is realized based on an AlScN straight waveguide, and the modulation efficiency is significantly enhanced by 12.3 dB through the extension of the AO interaction length and the utilization of bidirectional acoustic energy. The intermodal AO modulation and non-reciprocity are further demonstrated based on a multi-mode spiral waveguide, achieving a high non-reciprocal contrast (>10 dB) across an optical bandwidth of 0.48 nm. This research marks a significant stride forward, representing an advancement in the realization of microwave photonic filters, magnet-free isolators, and circulators based on the thin-film AlScN photonic platform. © 2024 Chinese Laser Press

<https://doi.org/10.1364/PRJ.517719>

## 1. INTRODUCTION

Electrically driven acoustic waves can induce a minuscule change in the material's refractive index, thereby modulating optical signals, including optical frequency, intensity, and propagation direction [1–3]. Leveraging this principle, a variety of applications covering optical frequency shifting [4–7], non-reciprocal optical transmission [8–12], beam deflection [13–15], and microwave filtering [16–19] have been achieved. Conventionally, acousto-optic (AO) modulators have relied on bulk piezoelectric materials, limiting their integration and modulation efficiency [20,21]. With the advancements in nanofabrication technology, significant progress has been made in the development of photonic integrated circuits (PICs) [22–24]. PICs can effectively confine optical waves within a waveguide structure and excite acoustic waves through piezoelectric thin-film materials, demonstrating high AO overlap in a small range to achieve efficient AO modulation. The acoustic waves required for modulation can be easily realized by excitation of surface acoustic waves (SAWs) through radio frequency (RF) driven interdigital electrodes (IDTs). SAWs are well

confined within the depth range of several acoustic wavelengths without suspended structures, making the devices more stable and feasible [21,25]. Therefore, utilizing SAWs to modulate the optical signals within the waveguide is one of the feasible methods to achieve efficient AO modulation.

Previous reports have demonstrated AO modulators based on piezoelectric films such as lead zirconate titanate (PZT) [26], gallium arsenide (GaAs) [27,28], gallium nitride (GaN) [29], lithium niobate (LN) [15,21,30], and polycrystalline aluminum nitride (AlN) [2,8,10,17,31]. Particularly, AlN films have the potential to realize high-performance AO modulators with low cost as their fabrication process is compatible with complementary metal-oxide-semiconductor (CMOS) technology [32,33]. In 2023, an integrated AO device based on a suspended AlN waveguide was reported, achieving intramodal AO modulation with a modulation efficiency of -34 dB [10]. Interestingly, the piezoelectric properties of AlN films can be significantly improved by doping scandium (Sc) elements, which has been widely demonstrated in the development of piezoelectric microelectromechanical systems (MEMS) [34–37]. Furthermore, recent researches indicate that AlScN

exhibits a wide electronic band gap close to that of the AlN, resulting in a wide transparent window from ultraviolet to mid-infrared [38,39]. Consequently, the integration of waveguides and IDTs using thin-film AlScN is a feasible strategy for achieving a high AO overlap in the modulation process. In 2020, Shiyang Zhu and others reported the first AlScN photonic circuits on a silicon substrate [40]. Our previous work further demonstrated AlScN microring resonators, where the AlScN film was deposited by physical vapor deposition (PVD) sputtering system on an 8-inch silicon wafer with 3- $\mu\text{m}$  silicon dioxide ( $\text{SiO}_2$ ) [41]. Therefore, the AlScN-on-insulator (AlScNOI) photonic platform that combines a large piezoelectric effect and a wide transparent window is expected to promote the further development of on-chip AO devices.

In this work, to the best of our knowledge, we present the first demonstration of AO modulators with SAWs generation and photonic waveguides monolithically integrated on a 400-nm-thick film of AlScN on an insulator. Experimental results show that the broadband ( $>20$  nm) intramodal AO modulation is achieved, and the modulation efficiency can be enhanced by placing IDTs in the center of a spiral waveguide, which utilizes 100% bidirectional acoustic energy in principle. The highest modulation efficiency of the AO modulator is  $-19.2$  dB with an RF drive power of 25 dBm and the RF 3-dB bandwidth is 5.9 MHz. Subsequently, we demonstrate intermodal AO modulation in a multi-mode waveguide, achieving non-reciprocal AO modulation with a high contrast ( $>10$  dB)

across an optical bandwidth of 0.48 nm in the communication wavelength range. At an RF power of 25 dBm, the highest modulation efficiency of the device is  $-15.9$  dB. Drawing upon the advantages of a CMOS-compatible process and effective AO modulation, those AO devices hold promise for advanced applications, particularly in narrowband microwave photonic filters, optical isolators, and circulators.

## 2. RESULTS

### A. AO Devices Based on Thin-Film AlScN Photonic Platform

The AO devices are fabricated using the thin-film AlScN photonic platform depicted in Fig. 1(a). This material platform enables the preparation of optical waveguides and efficient electromechanical transducers on the same film. Optical signals are coupled into and out of the AO devices through the grating couplers (the coupling loss is 9.02 dB per facet at 1550 nm), and the optical frequency shifts are induced by the AO modulation. Meanwhile, based on the device (top), non-reciprocity is investigated through intermodal AO modulation, with detailed discussions in Section 2.D. A cross-sectional view of the modulator is shown in Fig. 1(b). The 400-nm-thick polycrystalline AlScN is deposited on an 8-inch Si wafer with 3- $\mu\text{m}$   $\text{SiO}_2$  cladding from a pre-alloyed target (Sc:Al = 9.6%:90.4%, atomic percentage) in a PVD sputtering system. On the surface of the piezoelectric AlScN film, electrical contact pads and

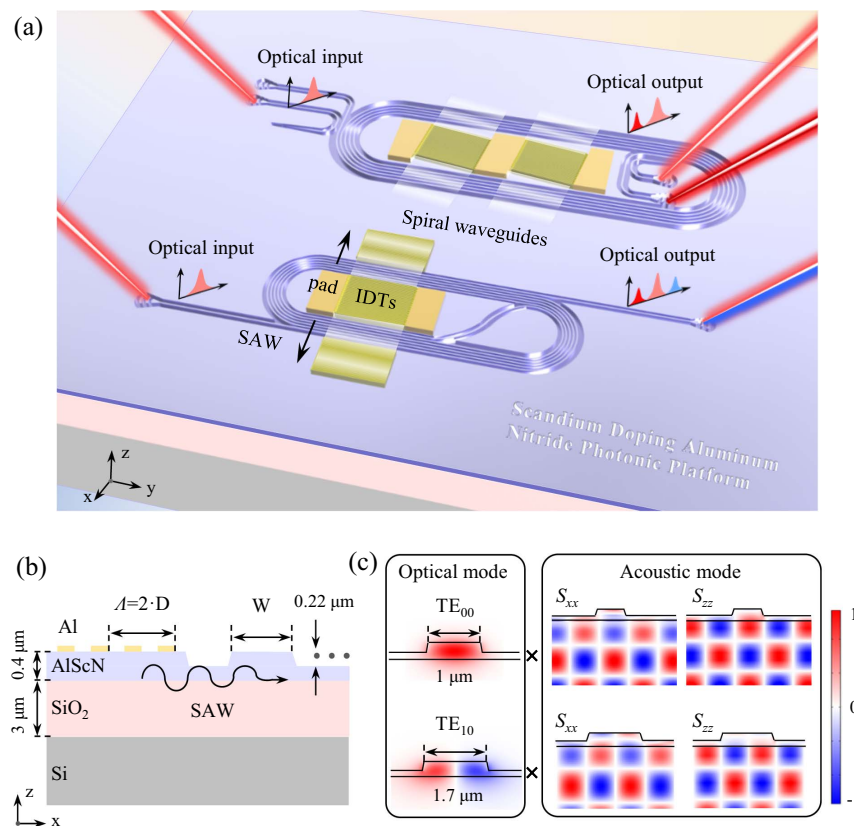


**Fig. 1.** AO devices based on thin-film AlScN photonic platform. (a) Schematic diagram of AO devices for intramodal AO modulation (bottom) and intermodal AO modulation (top). (b) Cross-sectional view of the device. It consists of an AlScN ridge waveguide with a width ( $W$ ) and an etching depth of 220 nm, along with the aluminum IDTs. (c) Numerical simulation results of the normalized electric field and strain field profiles.

IDTs consisting of interdigitated fingers with equal spacing are patterned using two lift-off processes with 100-nm-thick gold and 100-nm-thick aluminum, respectively. Electromechanical transduction of SAWs can be achieved by RF-driving IDTs. The optical ridge waveguides with different widths are fabricated by partial etching (etching depth  $d = 220$  nm) of the AlScN layer, and the sidewall angle is about  $70^\circ$ .

AO modulation originates from the change of the material's refractive index within the range of the optical mode field due to the time-harmonic strain field generated by the acoustic wave. A substantial spatial overlap of the acoustic strain field with the optical modes is considered a necessary condition for achieving efficient AO modulation. The numerical simulation results of the normalized field distribution of the optical mode and acoustic mode (strain field in  $x$  and  $z$  directions) are shown in Fig. 1(c). It can be seen that the fundamental transverse electric ( $TE_{00}$ ) optical mode is supported by a ridge waveguide with a top width of  $1 \mu\text{m}$ . The right side shows the strain profile in the cross-sectional area when SAWs with wavelength  $\Lambda = 2.2 \mu\text{m}$  (angular frequency  $\Omega = 2\pi \times 2.3$  GHz) propagate perpendicular to the waveguide. The first-order transverse electric ( $TE_{10}$ ) optical mode is supported by a multimode waveguide with a top width of  $1.7 \mu\text{m}$ . The right side shows the strain profile when SAWs with wavelength  $\Lambda = 1.88 \mu\text{m}$  ( $\Omega = 2\pi \times 2.8$  GHz) propagate at an angle of  $81.81^\circ$  to the waveguide. Here, the selection of acoustic waves with different wavelengths  $\Lambda$  and driving frequencies for achieving intramodal AO modulation ( $TE_{00}$ ) and intermodal AO modulation ( $TE_{10} - TE_{00}$ ) is determined through the optimizing of the AO overlap based on finite element simulations (more details are presented in Appendix A). Mathematically, this AO overlap is proportional to [2,4,17]

$$\Gamma = \frac{\iint E_2^*(x)E_1(x)(P'_{11}S_{xx} + P_{13}S_{zz})dx dz}{\left(\iint |E_1(x)|^2 dx dz \iint |E_2(x)|^2 dx dz\right)^{1/2}}, \quad (1)$$

where  $P'_{11}$  and  $P_{13}$  are the photoelastic coefficients,  $S_{xx}$  and  $S_{zz}$  are the strains in the  $x$  and  $z$  directions, and  $E_1(x)$  and  $E_2(x)$  are the  $x$ -component electric fields of the probe light and the scattered light, respectively.

### B. Characterization of AlScN Film

The properties of the AlScN film are characterized. The crystal orientation of the film is studied by X-ray diffraction (XRD), and the  $2\theta$  pattern is shown in Fig. 2(a). The strongest peak appears at  $36.6^\circ$ , indicating that the AlScN film is deposited along the preferred  $c$ -axis orientation (0002). Another strong peak appears at  $69^\circ$ , which reveals the crystal orientation of Si (004). In Fig. 2(b), the full width at half maximum (FWHM) of the AlScN film in the X-ray rocking curve is measured to be  $1.84^\circ$ , while the FWHM of AlScN films deposited on Si substrates is typically about  $2^\circ$  [34]. In order to assess the optical properties, we conducted spectral ellipsometry characterization of the AlScN film and characterized the morphology of the ridge waveguide using atomic force microscopy (AFM). Figure 2(c) shows the measured complex refractive indices (refractive index  $n$  and extinction coefficient  $k$ ) in the spectral range 600 to 1700 nm. The results indicate that its refractive index is larger than that of the AlN film due to the scandium

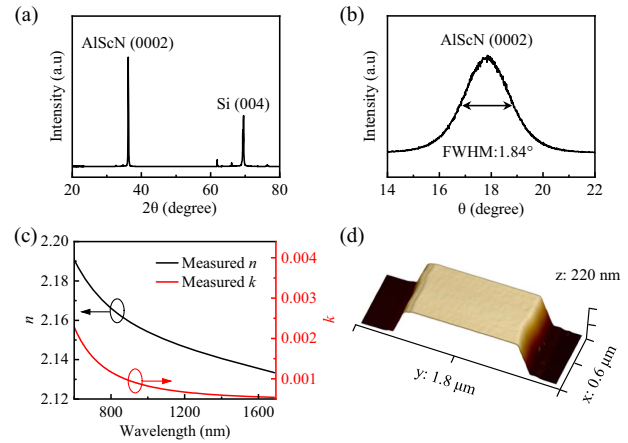


**Fig. 2.** Characterization of AlScN film. (a) XRD  $2\theta$  pattern indicates that the AlScN film is deposited along the  $c$ -axis-oriented (0002). (b) Rocking curve of the 0002 AlScN peak has a FWHM of  $1.84^\circ$ . (c) Measured refractive index  $n$  (black line) and extinction coefficient  $k$  (red line) as a function of optical wavelength. (d) AFM image of the ridge waveguide.

doping [42], reaching 2.13 at a wavelength of 1550 nm. Additionally, the measured extinction coefficient is below 0.0025 and decreases as the wavelength increases, gradually approaching zero. After fabrication, an AFM image taken on a ridge waveguide is shown in Fig. 2(d). The results show that the residual root-mean-square (rms) roughness on the top surface of the waveguide is 0.48 nm, and the surface rms roughness on the slab area is 0.52 nm.

### C. Intramodal AO Modulation

First, the basic structure consisting of a straight waveguide and IDTs shown in Fig. 3(a) is used to investigate intramodal AO modulation based on the AlScN platform. The optical insertion loss of the device is less than 0.9 dB, while the waveguide propagation loss is 8.11 dB/cm at the wavelength of 1550 nm. This loss is mainly due to the rough sidewall, which can be reduced through optimization of the etching process. Here, IDTs with pitch ( $D$ ) are used to excite SAWs with wavelength  $\Lambda = 2D = 2.2 \mu\text{m}$ , which is designed to match the optical modes for maximum AO overlap. These SAWs are incident normal to the optical propagation axis. Over an AO interaction length of  $L = 200 \mu\text{m}$ , the probe light guided in the  $TE_{00}$  mode at angular frequency  $\omega_a$  is scattered to frequency-detuned waves guided in the same optical mode at  $\omega_a \pm \Omega$ . Figure 3(b) illustrates the behavior of the intramodal AO modulator in the  $\omega - k$  space, where  $|k| = 2\pi/\lambda$  is the wavevector (the photon/phonon momentum is  $\hbar k$ ), and  $\omega$  is the angular frequency (the photon/phonon energy is  $\hbar\omega$ ). Phase matching for this AO scattering process requires that energy and momentum conservations should be satisfied. For Stokes (frequency decrease) and anti-Stokes (frequency increase) processes, the initial and final particle states need to satisfy the following equations [2]:

$$\text{Anti-Stokes: } k_{a_1} = k_a + q, \quad \omega_{a_1} = \omega_a + \Omega, \quad (2)$$

$$\text{Stokes: } k_{a_2} + q = k_a, \quad \omega_{a_2} + \Omega = \omega_a. \quad (3)$$

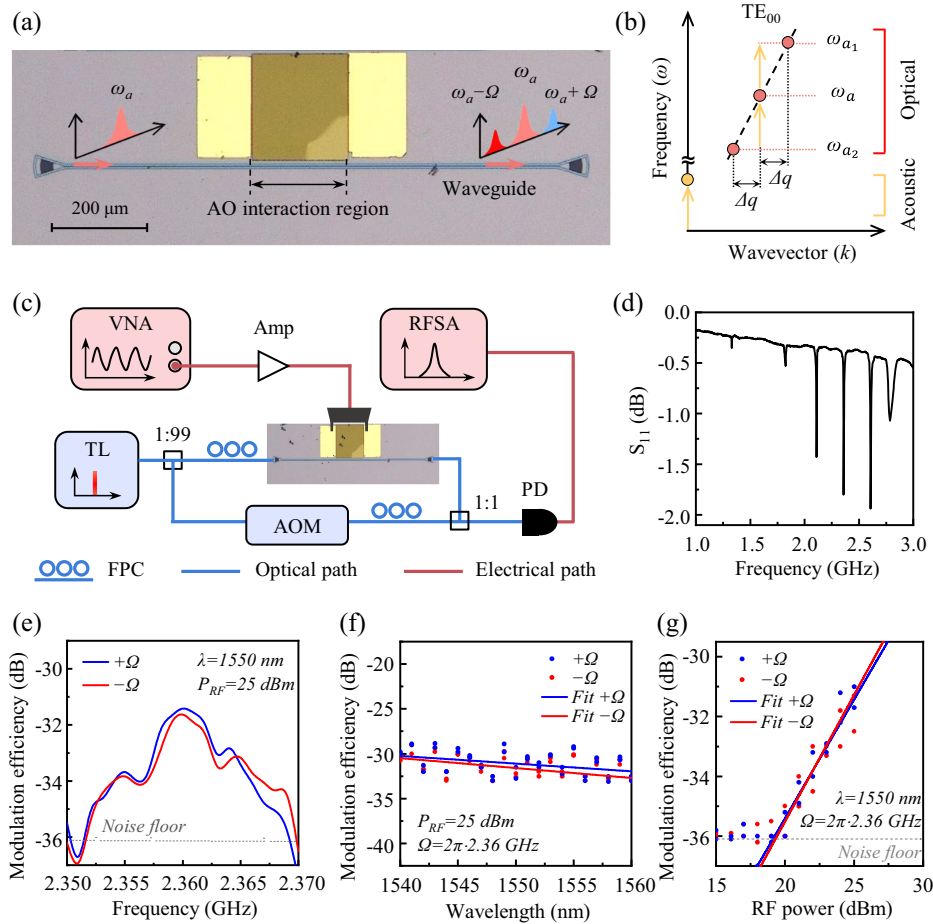


**Fig. 3.** Intramodal AO modulation based on an AlScN straight waveguide. (a) Micrograph of the fabricated AO modulator. (b) Schematic diagram of  $\omega - k$  space showing the phase matching condition. (c) Schematic diagram of the setup used to characterize the AO modulators. (d) Electrical reflection coefficient  $S_{11}$  as a function of RF frequency  $\Omega/2\pi$ . (e) RF frequency response of the measured modulation efficiency. (f) Modulation efficiency versus optical wavelength, with the RF frequency fixed at  $\Omega/2\pi = 2.36$  GHz. (g) Modulation efficiency versus RF power in the range of 15 to 25 dBm. The blue and red lines result from the linear fitting.

Since the IDTs excite acoustic waves with an axial acoustic wavevector ( $q = 0$ ), the scattering process is not exactly phase matched. But the mismatch  $\Delta qL = \Omega \partial k / \partial \omega L \approx 0.003$ , which is small enough that this scattering still occurs [2,4].

The experimental setup used to characterize the AO modulators is shown in Fig. 3(c). The probe light ( $\omega_a$ ) from the tunable laser (TL, Keysight 81634B) is split into two paths. In the lower path, 1% of the light passes through an AO frequency shifter (AOFs), which shifts the optical angular frequency to  $\omega_a + \Delta$  (where  $\Delta = 2\pi \times 200$  MHz) as a frequency-detuned local oscillator for heterodyne detection. Meanwhile, in the upper path (99% of the light), the light is coupled to the device coupler after controlling the polarization with a fiber polarization controller (FPC). The RF signal with an angular frequency of  $\Omega$  provided by the vector network analyzer (VNA, Keysight ENA E5071C) is amplified by the RF amplifier (Amp, Mini-Circuits ZHL-5W-63-S+) and then drives the IDTs to generate SAWs. In the device, part of the light is scattered to the optical sidebands with angular frequencies of  $\omega_a \pm \Omega$ . After being coupled off-chip, the output optical signals are combined with the local oscillator

(controlled to the same polarization as the upper path light through another FPC) and incident on a photodiode (PD, Thorlabs RXM10AF), generating an RF beat tone that is detected by an RF spectrum analyzer (RFSa, R&S FPL1014). The beat tones are at  $\Omega \pm \Delta$  for  $\mp\Omega$ -shifted sidebands and at  $\Delta$  for unshifted light, where the RF power shown in the RFSa is proportional to the optical power in the corresponding beat tone. Therefore, the AO modulation efficiency, defined as the ratio of the scattered optical sideband power to the incident probe power  $\eta = 10 \log_{10}[P_{\text{out}}(\omega_a \pm \Omega)/P_{\text{out}}(\omega_a)]$ , can be obtained by analyzing the RF power ratio of the corresponding beat tones.

The electrical reflection coefficient  $S_{11}$  of the IDTs is plotted in Fig. 3(d) as a function of RF frequency. Over the wide-band RF frequency, there are several strong SAW modes actuated at the different frequencies. The experiments confirm that the actuated SAW mode at a frequency of 2.36 GHz obtains the largest AO modulation efficiency with the probe light at a wavelength of  $\lambda = 1550$  nm. According to the conversion efficiency formula from RF power to SAW power  $\eta_{\text{IDT}} = \Delta |S_{11}|^2$  [43], the conversion efficiency of the IDTs at the

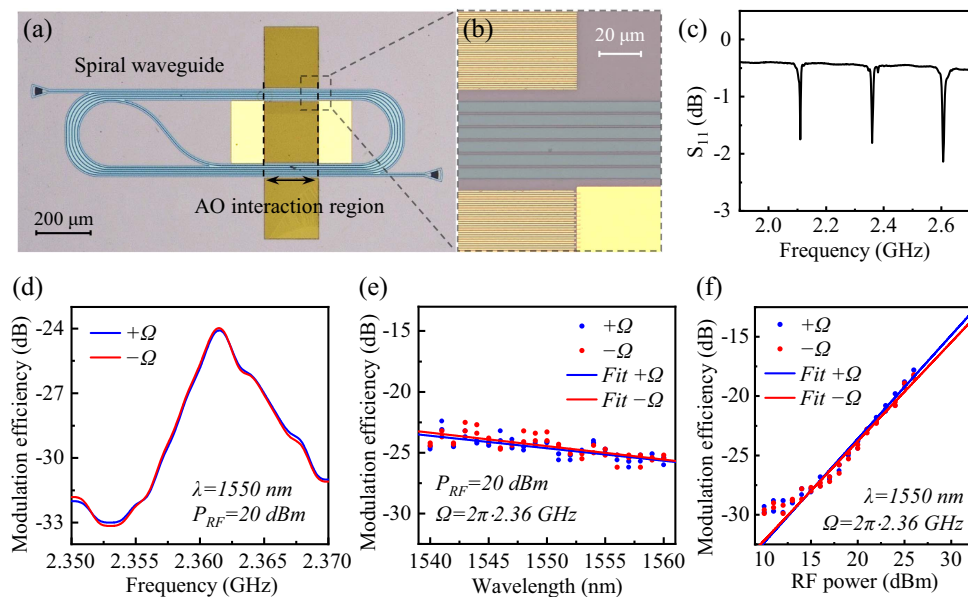
RF drive frequency  $\Omega/2\pi$  of 2.36 GHz is 25.6%. More details on IDTs' performance are presented in Appendix B. The RF frequency response of the measured modulation efficiency is plotted in Fig. 3(e) with an RF drive power of  $P_{RF} = 25$  dBm. The blue line and the red line represent the anti-Stokes process and Stokes process, respectively. The peak modulation efficiency is  $-31.5$  dB with a 3-dB bandwidth of 12.7 MHz at the RF central frequency  $\Omega/2\pi$  of 2.36 GHz, consistent with the resonant valley of  $S_{11}$  in Fig. 3(d).

Figure 3(f) shows the measured modulation efficiency (blue dots/red dots) over the optical wavelength range of 1540–1560 nm. Blue and red points denote the anti-Stokes process and Stokes process, respectively, and the blue line and red line are linear fittings of the measured results. As the phase matching conditions are fulfilled across the broadband wavelength range, the device achieves broadband AO modulation. As the wavelength increases, the modulation efficiency decreases slightly, which is mainly due to the slight change in the polarization of the local oscillator light caused by the changing of wavelength. At the same time, the AO modulation efficiency is theoretically proportional to the square of the optical frequency [9]. The power dependence of the modulation efficiency is shown in Fig. 3(g), revealing that the power of the scattered light at the  $\pm\Omega$  sidebands is linearly correlated with the RF drive power.

In order to take full advantage of the SAWs' power and enhance the modulation efficiency, an intramodal AO modulator with IDTs placed in the center of a spiral waveguide shown in Figs. 4(a) and 4(b) is further demonstrated. Another 50 pairs of interdigital electrodes with the same period serve as an SAW reflector patterned behind the waveguides to increase the modulation efficiency by forming acoustic resonant cavities. The area and total length of the compact spiral waveguide

are  $1240 \mu\text{m} \times 310 \mu\text{m}$  and  $15,500 \mu\text{m}$ , respectively. The optical insertion loss of the device is 14.6 dB. Figure 4(c) shows the electrical reflection coefficient  $S_{11}$  of IDTs over an RF frequency range. The maximum AO modulation efficiency occurs near 2.36 GHz and the conversion efficiency of the IDTs is 24.0%. In the presence of SAWs, the probe light is scattered to the sidebands in the 11 segments of the interaction region, corresponding to the equivalent AO interaction length of  $L_{eq} = 11 \times 200 \mu\text{m}$ . The modulated light in each interaction segment interferes with each other, and the final amplitude of the modulated light is the superposition of all modulation amplitudes with optical and acoustic phase differences. Since the effective refractive index difference between the probe light and the modulated light is small, the impact of the optical phase difference ( $<0.084\pi$ ) on the modulation efficiency is negligible [4]. Moreover, the lateral distance between adjacent interaction segments is designed to be an integer multiple of the acoustic wavelength  $\Lambda$  to control the acoustic phase difference of each interaction segment to be approximately an integer multiple of  $2\pi$ . However, since the lateral distance of the spiral waveguide is much larger than the wavelength of the SAWs, and it is challenging in fabrication to achieve the same spacing between the IDTs and the waveguides on both sides, the modulation efficiency of the device is mainly affected by the acoustic phase difference.

The RF frequency response of measured modulation efficiency in the spiral waveguide, with a probe wavelength of  $\lambda = 1550$  nm and an RF drive power of  $P_{RF} = 20$  dBm, is plotted in Fig. 4(d). The strongest peak is  $-24$  dB at RF drive frequency  $\Omega/2\pi$  of 2.36 GHz with a 3-dB bandwidth of 5.9 MHz. Figure 4(e) shows that the device achieves optical broadband AO modulation, and the measured modulation efficiency variation is within  $\pm 2$  dB in the wavelength range of



**Fig. 4.** Intramodal AO modulation with enhanced modulation efficiency based on an AlScN spiral waveguide. Micrographs of the intramodal AO modulator at various levels of detail are shown in (a) and (b). (c) Electrical reflection coefficient  $S_{11}$  as a function of RF frequency  $\Omega/2\pi$ . (d) RF frequency response of the modulation efficiency for the AO modulator. (e) Modulation efficiency versus optical wavelength, with the RF frequency fixed at  $\Omega/2\pi = 2.36$  GHz. (f) Modulation efficiency versus RF power in the range of 15 to 25 dBm.

1540–1560 nm. As shown in Fig. 4(f), the modulation efficiency of the device is linearly related to the RF drive power within the RF power range of 15–25 dBm. Under the same RF drive power of 25 dBm, the modulation efficiency of the device is increased by 12.3 dB, and this value can be improved by further optimizing the acoustic phase.

#### D. Intermodal AO Modulation and Non-reciprocity

By designing the direction of IDTs to achieve a non-zero axial acoustic wavevector, intermodal AO modulation based on a multi-mode optical waveguide is demonstrated. This process scatters light between different optical modes ( $TE_{00}$  –  $TE_{10}$ ) with acoustic wavevector selectivity, enabling non-reciprocal AO modulation. Figure 5(a) shows the behavior of the non-reciprocal AO modulator in the  $\omega - k$  space. For light ( $\omega_a$ ) injected into the  $TE_{10}$  mode in the backward direction, the

process of mode conversion to  $TE_{00}$  mode and angular frequency shift to  $\omega_a - \Omega$  is phase matched, and the axial wavevector (forward) of the acoustic wave is  $|q_{\text{propagation}}| = |k(TE_{00}, \omega_a - \Omega) - k(TE_{10}, \omega_a)|$ . However, for light injected in the forward direction into the  $TE_{10}$  mode at the same frequency, the non-zero group velocity of the  $TE_{00}$  mode leads to an asymmetric wavevector mismatch  $\Delta q = |k(TE_{00}, \omega_a - \Omega) - k(TE_{00}, \omega_a + \Omega)|$ . Due to this phase mismatch, forward and backward lights passing through the device exhibit different modulation efficiencies.

To study the intermodal AO modulation, a spiral multi-mode optical waveguide is connected with asymmetric directional couplers (ADCs) to route scattered light [44–46], as shown in Fig. 5(b). In the input part, the probe light injected into port 1 is coupled into the multi-mode waveguide through

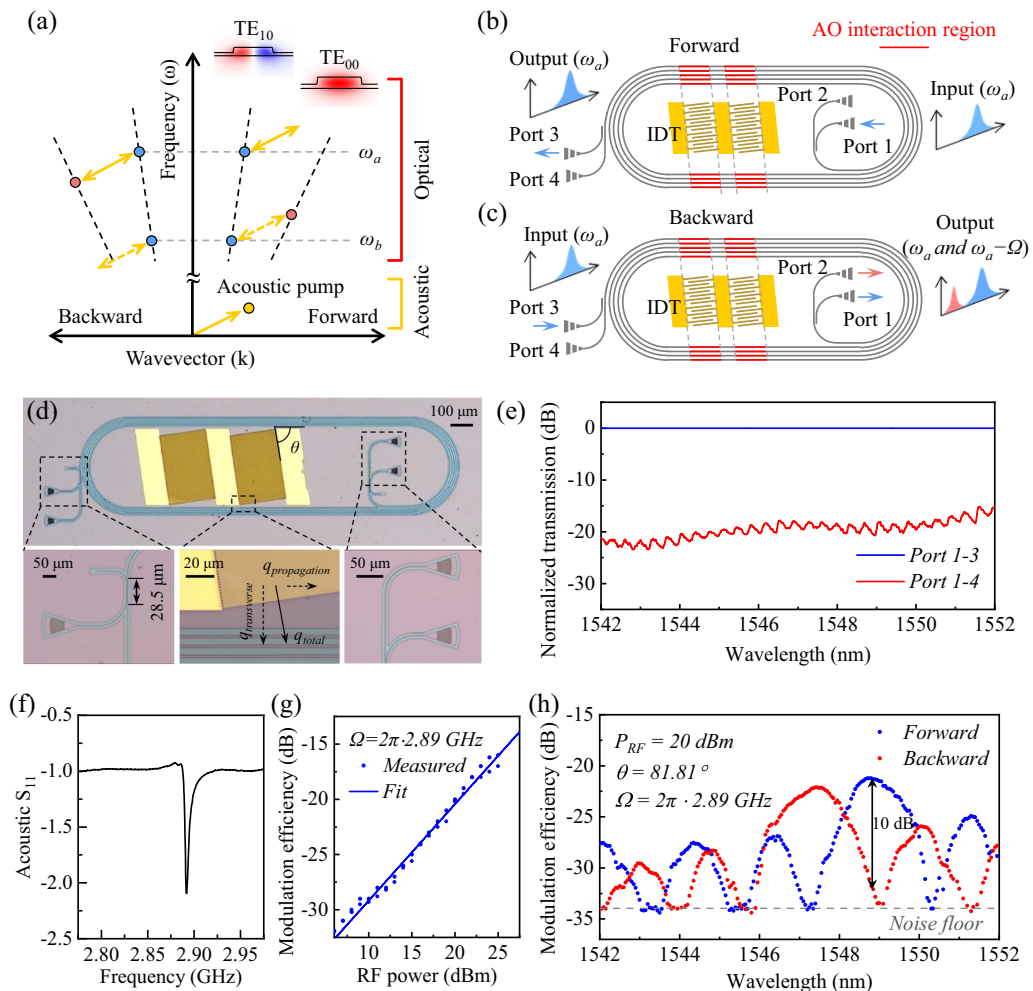


**Fig. 5.** Intermodal AO modulation in a multi-mode AlScN waveguide. (a) Schematic diagram of  $\omega - k$  space showing the intermodal AO modulation phase matching condition. (b) In the forward direction, the probe light (blue) travels through the device without alteration. (c) In the backward direction, the intermodal AO modulation is phase matched, such that the probe light is partly converted to the  $TE_{00}$  mode and is output in port 2 (red). (d) Micrograph of the fabricated intermodal AO modulator. The zoomed-in images below show details of the ADC, IDTs, and grating couplers. (e) Normalized optical transmission of the device without being RF driven. (f) Electrical reflection coefficient  $S_{11}$  as a function of RF frequency for IDTs with pitch  $D = 0.94 \mu\text{m}$ . The conversion efficiency of the IDTs at the RF drive frequency  $\Omega/2\pi$  of 2.89 GHz is 17.9%. (g) Modulation efficiency versus RF power in the range of 15 to 25 dBm. The blue line results from linear fitting indicating the linear relationship between the modulation efficiency and RF power. (h) Modulation efficiency versus optical wavelength. The blue dots (forward) and red dots (backward) represent the measured data.

the ADC, and the optical mode changes to TE<sub>10</sub>. After propagating through the spiral waveguide, the light couples via another ADC and outputs directly from port 3. Due to the reversibility of the optical path, this process also occurs in the backward direction (probe light is input from port 3 and output from port 1). Figure 5(c) shows the process of AO modulation. Probe light ( $\omega_a$ ) is injected into port 3 and coupled into the TE<sub>10</sub> mode in the spiral waveguide. SAWs with frequency  $\Omega/2\pi$  that are propagating at an obtuse angle relative to the probe light ( $q < 0$ ) are incident in the AO interaction regions. Through the intermodal AO modulation processes, probe light is mode-converted to the TE<sub>00</sub> mode and frequency-shifted to  $\omega_a - \Omega$ . Afterwards, probe light and modulated light are split through an ADC, which couples light remaining in the TE<sub>10</sub> mode out of port 1 and mode-converted light in the TE<sub>00</sub> mode out of port 2.

Figure 5(d) shows the photographs of the AO device. The experimental results show that the ADCs achieve good mode conversion. Figure 5(e) shows the normalized optical transmission of the device without RF drive power in the optical wavelength range of 1542–1552 nm. The incident light enters through port 1 and exits from port 3, while the light output from port 4 has an extinction ratio  $>15$  dB. The electrical reflection coefficient  $S_{11}$  of the IDTs is plotted in Fig. 5(d) as a function of RF frequency. SAWs are excited at a frequency of 2.89 GHz. In order to achieve intermodal modulation of the device near the optical wavelength of 1550 nm, an acoustic propagation constant of  $q_{\text{propagation}} = 4.76 \times 10^5 \text{ m}^{-1}$  is required to satisfy momentum conservation in the propagating direction. And the cross-sectional AO overlap is maximized when the transverse acoustic wavelength is 1.9  $\mu\text{m}$ , setting the transverse propagation constant to  $q_{\text{transverse}} = 2\pi/1.9 \mu\text{m} = 3.31 \times 10^6 \text{ m}^{-1}$ . Considering both the transverse and propagating components of the acoustic wave, the total wavevector of the acoustic wave emitted by the IDTs is calculated as  $q_{\text{total}} = (q_{\text{propagation}}^2 + q_{\text{transverse}}^2)^{1/2} = 3.85 \times 10^6 \text{ m}^{-1}$ . Therefore, the pitch of the IDTs is set to  $D = \Lambda/2 = \pi/q_{\text{total}} = 0.94 \mu\text{m}$ , and the angle between IDTs and the waveguide is set to  $\theta = \arctan(q_{\text{transverse}}/q_{\text{propagation}}) = 81.81^\circ$ .

The measured setup for the device is the same as mentioned in Section 2.C. The output ports 3 and 4 (ports 1 and 2 for backward direction) of the device are combined with the local oscillator and the output light is incident on a PD, producing an RF beat tone that is detected by an RFSA. The AO modulation efficiency of the modulator

can be expressed as  $\eta = 10 \log_{10}((P_{\text{out}}(\omega_a \pm \Omega)/P(\omega_a + \Delta)) \times (P_{\text{out}}(\omega_a)/P(\omega_a + \Delta)))$  [47]. As shown in Fig. 5(g), the measured modulation efficiency is plotted as a function of RF power in the range of 15 to 25 dBm, and the maximum modulation efficiency of the device is  $-15.9$  dB.

It is worth noting that, owing to the different optical group velocities of the two optical modes, light propagating forward can also fulfill the phase matching condition of the intermodal modulation process at other frequencies ( $\omega_b$ ), as shown by the dashed arrow in Fig. 5(a). The frequency difference for forward and backward phase matching can be calculated by linearizing the optical dispersion:  $\omega_a - \omega_b = 2\pi \times 199.05$  GHz. The non-reciprocal response of the AO modulator is experimentally demonstrated by fixing the RF frequency at 2.89 GHz and setting the RF drive power to 20 dBm. The probe light is injected into the forward (port 1) and backward (port 3) directions. In Fig. 5(h), the modulation efficiency is shown as a function of optical wavelength. Over the communication wavelength range, the device achieves non-reciprocal AO modulation at multiple optical wavelengths, consistent with the theoretical wavelength-dependent AO modulation of the device (Appendix C). At the central wavelength of 1548.7 nm, the device exhibits a non-reciprocal contrast of more than 10 dB over a bandwidth of 0.48 nm. Looking ahead, the AO modulation efficiency of the device can be enhanced by increasing the AO interaction length and improving the RF-driven power. When the device achieves near unity energy conversion, it can be used as a two-port optical isolator (ports 1 and 3) and a three-port frequency-shifted optical circulator (ports 1, 2, and 3).

### 3. DISCUSSION

We demonstrated the AO modulators with SAWs generation and photonic waveguides monolithically integrated on AlScN film on an insulator. We compare the device with other reported integrated AO modulators in different platforms as shown in Table 1. With superior piezoelectric properties [34], our AlScN devices, which do not require suspended structures, exhibit higher AO modulation efficiency and improved mechanical stability compared to the reported AO modulators based on the AlN platform [10,48].

Gallium nitride (GaN) is another candidate for AO modulation, with a piezoelectric coefficient ( $d_{33}$ ) of  $3.5 \text{ pC}\cdot\text{N}^{-1}$  [49]. Recent work has demonstrated complete optical conversion with integrated AO modulators based on the GaN on sapphire platform [50]. However, unlike our AlScN photonic

**Table 1. Benchmark of AO Modulator Performances**

Platform	Suspended	Acoustic Frequency	Modulation Type	Modulation Efficiency (RF Power)	RF 3-dB Bandwidth	Year
AlN	Y	16.4 GHz	Intermode	-56 dB (20 dBm)	31 MHz	2019 [48]
AlN	Y	5.07 GHz	Intramode	-34 dB (20 dBm)	80 MHz	2023 [10]
GaN/sapphire	N	0.99 GHz	Intermode	-0.86 dB (27.5 dBm)	N.A.	2024 [50]
LNOI	N	2.89 GHz	Gaussian beam	-14.6 dB (30 dBm)	70 MHz	2020 [7]
LNOI	Y	0.44 GHz	Intermode	-14.6 dB (3 dBm)	N.A.	2021 [5]
AlScNOI	N	2.36 GHz	Intramode	-31.5 dB (25 dBm)	12.7 MHz	This work
AlScNOI <sup>a</sup>	N	2.36 GHz	Intramode	-19.2 dB (25 dBm)	5.9 MHz	This work
AlScNOI <sup>a</sup>	N	2.89 GHz	Intermode	-15.9 dB (25 dBm)	N.A.	This work

<sup>a</sup>Extending the acousto-optic interaction length using a spiral waveguide.

platform, the fabrication process of the GaN on sapphire platform is not compatible with CMOS technology, which restricts its potential for large-scale fabrication.

The lithium niobate-on-insulator (LNOI) platform has been extensively studied due to its excellent optical and piezoelectric ( $d_{33} = 6 \text{ pC}\cdot\text{N}^{-1}$ ) properties [51]. Previous studies have demonstrated AO modulators based on the LNOI platform with a modulation efficiency of  $-14.6 \text{ dB}$  [5,7]. Despite these achievements, the fabrication process of LNOI wafers is complex and expensive, posing challenges for large-scale production. Looking forward, by using AlScN with higher Sc concentrations, such as  $\text{Al}_{0.57}\text{Sc}_{0.43}\text{N}$ , which exhibits a piezoelectric coefficient  $d_{33}$  of  $27.6 \text{ pC}\cdot\text{N}^{-1}$  [34], devices are expected to achieve more efficient AO modulation.

Referring to the acoustic propagation losses in reported works [2,4], the total acoustic loss is estimated to be around  $1 \text{ dB}$  considering a maximal length of  $50 \text{ }\mu\text{m}$  along the direction of acoustic propagation in our device. Further reduction of acoustic propagation loss will benefit device performance for practical applications. A trade-off exists in adopting higher Sc concentration for the AO modulator. The piezoelectric coefficient  $d_{33}$  of the film increases with the Sc concentration when it is below  $43\%$  [34]. For mechanical properties, AlScN films are stable and can be used in applications involving high temperatures [52]. However, film and waveguide sidewall quality will degrade, resulting in higher optical losses [41,53]. This can be mitigated by further optimization of the fabrication process such as film deposition and etching process improvement.

#### 4. CONCLUSION

In summary, we demonstrate the intramodal and intermodal AO modulation based on a thin-film AlScN photonic platform. Experimental results show that when  $25\text{-dBm}$  RF drive power is applied, the modulation efficiency of the intramodal AO modulator at  $1550 \text{ nm}$  wavelength is  $-31.2 \text{ dB}$ , and the RF  $3\text{-dB}$  bandwidth is  $12.7 \text{ MHz}$ . To further improve the performance of the device, we propose an AO modulator by placing IDTs in the center of the spiral waveguide, which utilizes  $100\%$  bidirectional acoustic energy in principle. At the same RF drive power, the modulation efficiency is up to  $-19.2 \text{ dB}$  and the RF  $3\text{-dB}$  bandwidth is narrowed to  $5.9 \text{ MHz}$ . Combining a CMOS-compatible process and efficient AO modulation, our devices are expected to achieve advanced performance in on-chip frequency shifters and narrowband microwave photonic filters. Furthermore, we demonstrate the intermodal AO modulation and non-reciprocity in a multi-mode optical waveguide by designing the axial acoustic wavevector. In the communication wavelength range, the device achieves a high non-reciprocal contrast ( $>10 \text{ dB}$ ) over an optical bandwidth of  $0.48 \text{ nm}$ . At an RF drive power of  $25 \text{ dBm}$ , the maximum modulation efficiency of the device is  $-15.9 \text{ dB}$ .

In the future, the modulation efficiency of the device can be significantly improved by increasing the AO interaction length, optimizing impedance matching, and designing acoustic waves with strong AO coupling. As the modulation efficiency of this device is further improved, it is expected that time-reversal symmetry can be broken without magneto-optical materials, enabling broadband optical isolators and circulators.

#### APPENDIX A: NUMERICAL STUDY OF THE AO OVERLAP

The spatiotemporal variation in the refractive index modulation, induced by acoustic waves through a time-harmonic strain field, results in AO modulation. The alteration in the material's refractive index, caused by the strain field  $S$ , primarily stems from the photoelastic effect, expressed by the formula [54]

$$\Delta n_i = -\frac{1}{2} n_i^3 \sum_{jk} P_{ij} S_{jk}. \quad (\text{A1})$$

Here,  $S_{jk}$  is the strain tensor and  $P_{ij}$  is the elasto-optic coefficient tensor. In our simulation for the AlScN film with a low Sc concentration, we substitute  $P_{ij}$  with the photoelastic coefficients of AlN:  $P_{11} = -0.1$ ,  $P_{33} = -0.107$ ,  $P_{12} = -0.027$ ,  $P_{13} = -0.019$ ,  $P_{44} = -0.032$ , and  $P_{66} = -0.037$  [17]. Given the polycrystalline nature of the film, the in-plane elasto-optic coefficients are approximated as the average of the  $a$ - and  $b$ -direction coefficients:  $P'_{11} = (P_{11} + P_{12})/2 = -0.063$  [17]. Other parameters of the AlScN films used in the simulations are extracted from the reported data and are detailed in Table 2.  $P$  is the material density,  $C_{ij}$  is the elastic constants,  $e_{ij}$  is the piezoelectric coefficients,  $\epsilon_p$  is the dielectric constant, and  $\epsilon_0$  is the vacuum dielectric constant.

To quantify the extent of AO interactions of AO modulators, finite element simulations were employed to calculate the spatial AO overlap between acoustic and light fields in the cross-section. Ignoring the shear components of the strain field tensor ( $S_{xy}$ ,  $S_{yz}$ ,  $S_{xz}$ ), which are much weaker than the normal components, this overlap can be approximated by calculating Eq. (1). The simulation involved alterations of parameters, including the wavelength and frequency of SAWs. As shown in Fig. 6(a), for the intramodal AO modulation ( $\text{TE}_{00}$ ), when the acoustic wave wavelength is  $2.2 \text{ }\mu\text{m}$ , the acoustic and light overlap is maximum. As shown in Fig. 6(b), for the process of scattering from  $\text{TE}_{10}$  mode to  $\text{TE}_{00}$  mode (intermodal AO modulation), when the acoustic wave wavelength is  $1.88 \text{ }\mu\text{m}$ , the acoustic and light overlap on the cross-section is maximum. This serves as a guiding principle for optimizing the efficiency of our AO modulator.

#### APPENDIX B: CHARACTERIZATION OF THE INTER-DIGITATED SAW TRANSDUCER

IDTs with pitch  $\Lambda = 1.1 \text{ }\mu\text{m}$  are fabricated in a  $100\text{-nm}$ -thick Al metal layer on top of thin-film AlScN, achieving efficient

**Table 2. Parameters of the AlScN Films Used in the Simulations [36]**

$P$ ( $\text{g}/\text{cm}^3$ )	$C_{11}$ (GPa)	$C_{12}$ (GPa)	$C_{13}$ (GPa)	$C_{33}$ (GPa)	$C_{44}$ (GPa)	$e_{15}$ ( $\text{C}/\text{m}^2$ )	$e_{31}$ ( $\text{C}/\text{m}^2$ )	$e_{33}$ ( $\text{C}/\text{m}^2$ )	$\epsilon_p/\epsilon_0$
3.52	335	129	105	300	104	-0.32	-0.48	1.6	9.6

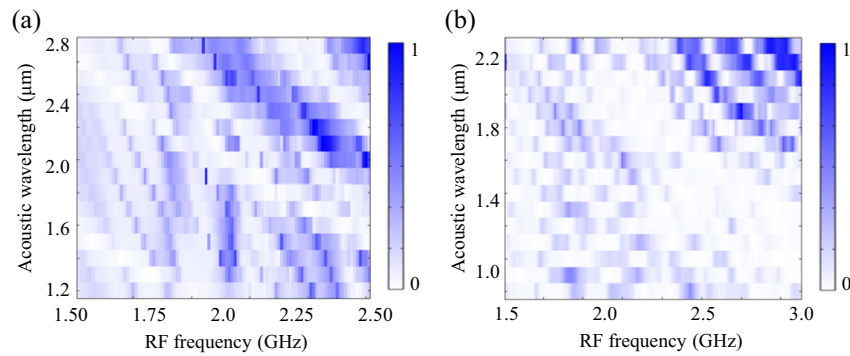


**Fig. 6.** Normalized finite element simulation results of AO overlap for the process of (a) intramodal AO modulation and (b) intermodal AO modulation, respectively.

electromechanical conversion of SAWs. The micrograph of IDTs is shown in Fig. 7(a). Its electromechanical response can be described by the Mason equivalent circuit model [55], where the IDTs' response consists of the static capacitance  $C$  of the interdigital array and the radiation impedance resulting from coupling with the SAWs. The total electrical admittance is given by

$$Y = 2\pi i f C + G_a(f) + iB_a(f), \quad (\text{B1})$$

where the radiation conductance  $G_a(f)$  and motional susceptance  $B_a(f)$  comprise the electromechanical response, and are given by

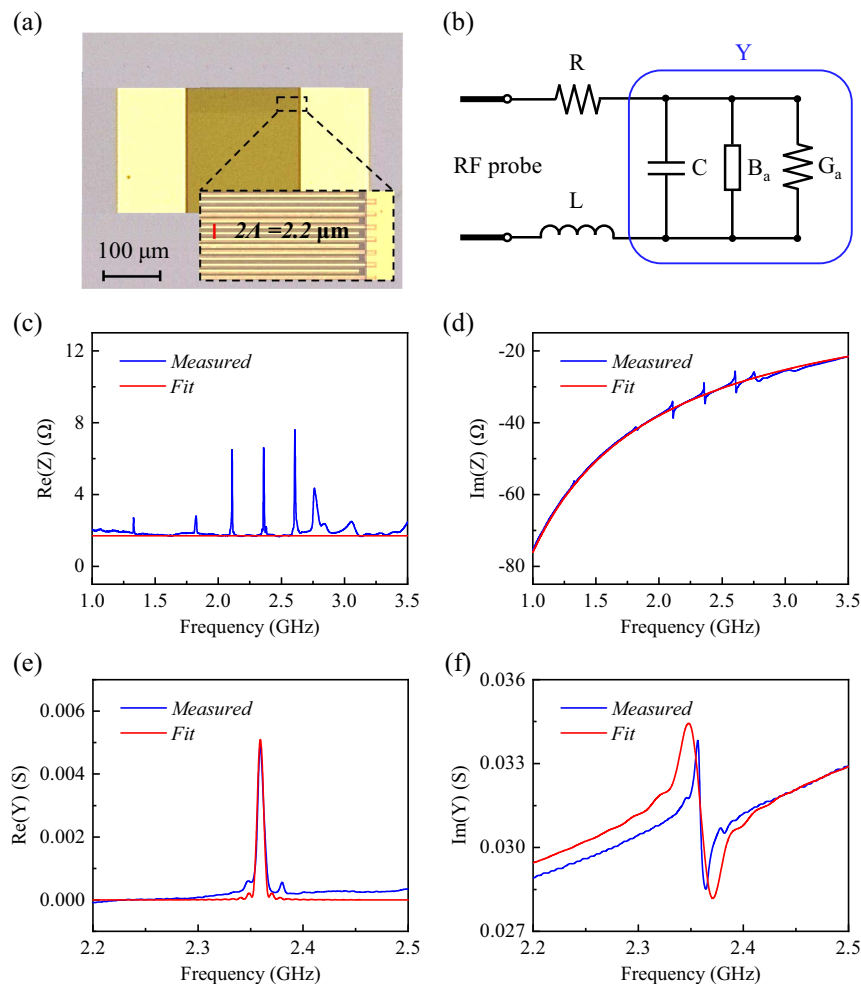


**Fig. 7.** (a) Micrograph of IDTs with pitch  $\Lambda = 1.1 \mu\text{m}$ . (b) Schematic diagram of the equivalent circuit model. Measured wideband (c) real part of impedance and (d) imaginary part of impedance with fitting curve (red line) as functions of frequency. Measured narrowband (e) real part and (f) imaginary part of admittance with fitting curve (red line) as functions of RF frequency.

$$G_a(f) = 8NCf_0K^2 \left( \frac{\sin\left(\frac{N\pi(f-f_0)}{f_0}\right)}{N\pi\left(\frac{f-f_0}{f_0}\right)} \right)^2, \quad (\text{B2})$$

$$B_a(f) = \frac{8NCf_0K^2 \left( \sin\left(\frac{N\pi(f-f_0)}{f_0}\right) - \frac{2N\pi(f-f_0)}{f_0} \right)}{2 \left( \frac{N\pi(f-f_0)}{f_0} \right)^2}. \quad (\text{B3})$$

In these equations,  $f_0$  is the center frequency,  $K^2$  is the material electromechanical coupling coefficient, and  $N$  is the number of transducer finger pairs. Furthermore, for interdigitated fingers with equal spacing,  $C$  can be calculated as [2]

$$C = NW(\epsilon_0 + \epsilon_p), \quad (\text{B4})$$

where  $W$  is the transducer width (aperture) given by the finger overlap length that is designed for 200  $\mu\text{m}$  and  $\epsilon_p$  is the effective permittivity of the substrate. It can be deduced from the experimental results that the effective permittivity of AlScN  $\epsilon_p \approx 9.6\epsilon_0$ , a capacitance per finger pair of  $C/N = 0.021$  pF, or around  $C = 2.12$  pF for a transducer with  $N = 100$ .

The parasitic resistance  $R$  and parasitic inductance  $L$  of the IDTs can be captured by the equivalent circuit model of Fig. 7(b). Using a calibrated electrical vector network analyzer, the total impedance  $Z$  of IDTs is measured as a function of frequency, as plotted in Figs. 7(c) and 7(d). These wideband data are fit to determine  $L$ ,  $C$  (imaginary part of  $Z$ ), and  $R$  (real part of  $Z$ ). As a result, we measure values of  $R = 1.98 \Omega$ ,  $C = 2.12$  pF, and  $L = 0.05$  nH for the transducer with pitch  $\Lambda = 1.1 \mu\text{m}$ . Narrowband impedance measurements of  $Y$  are shown in Figs. 7(e) and 7(f), which is used to determine the electromechanical coupling coefficient  $K^2$ . For the device,  $K^2 = 0.15\%$  at  $f_0 = 2.36$  GHz. Since the resonant peaks are quite sharp and the frequency scanning steps in the experiments may not be small enough, the measured values of  $K^2$  are smaller than the real values [4]. The  $K^2$  is mainly limited by the loosely confined acoustic wave (mostly in the oxide). In next steps, using AlScN with higher Sc concentrations and growing a layer of high-speed sound material (such as aluminum oxide) on the wafer before growing the AlScN film can help to greatly enhance it.

## APPENDIX C: WAVELENGTH RESPONSE OF THE NON-RECIPROCAL AO MODULATION

For given SAWs with frequency  $\Omega = 2.89$  GHz, we assume phase matching occurs when AO scattering takes place at the optical frequency  $\omega_a$  of the TE<sub>10</sub> mode. When the light frequency is detuned from  $\omega_a$ , the phase matching of the AO modulation process is no longer accurately satisfied. We can obtain an approximate wavevector mismatch  $\Delta q$  by linearizing the equation [2]

$$\Delta q = \frac{n_g(\text{TE}_{00}) - n_g(\text{TE}_{10})}{c} \Delta\omega, \quad (\text{C1})$$

where  $n_g(\text{TE}_{00}) = 3.84$  and  $n_g(\text{TE}_{10}) = 3.72$  are the group refractive indices of the TE<sub>00</sub> and TE<sub>10</sub> modes, respectively, and  $\Delta\omega$  is the light frequency detuned.

The total length of the multi-mode waveguide in the non-reciprocal AO modulator is  $L_{\text{total}} = 17.1$  mm. However, due to limitations imposed by the aperture of the IDTs, the length of the AO interaction is much shorter than this total length  $L_{\text{ao}} = 0.2 \times 18$  mm. In the following numerical study, we investigate the behavior of the modulator. The total modulation efficiency  $\eta$  of the device is related to the integral phase mismatch over the propagation length  $L_{\text{total}}$ , given by [12]

$$\eta(L) \propto \left( \int_0^L g_{\text{ao}}(z) e^{i\Delta q z} dz \right)^2, \quad (\text{C2})$$

where  $g_{\text{ao}}$  is the AO coupling strength. As shown in Fig. 8(a), it is assumed here that the AO coupling strength of the device is non-zero in the AO interaction regions and is zero in other regions. This type of device design results in the narrowband  $\text{sinc}^2$  non-reciprocal response, as shown by the blue line in Fig. 8(b). Owing to the different optical group velocities of the two optical modes, light propagating in the opposite direction can also fulfill the phase matching condition of the intermodal modulation process at other frequencies ( $\omega_b$ ). The frequency difference for forward and backward phase matching can be calculated by linearizing the optical dispersion [2]:

$$\omega_a - \omega_b = \Omega \left( \frac{n_g(\text{TE}_{00}) + n_g(\text{TE}_{10})}{n_g(\text{TE}_{00}) - n_g(\text{TE}_{10})} \right) = 2\pi \times 199.05 \text{ GHz}. \quad (\text{C3})$$

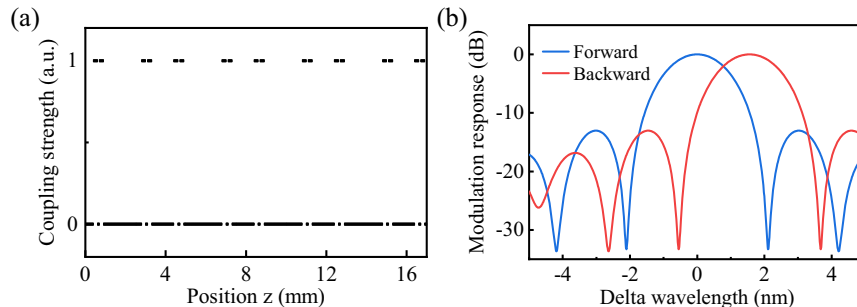


**Fig. 8.** Response of the non-reciprocity AO modulator, where AO coupling occurs over 18  $\mu\text{m} \times 200 \mu\text{m}$  regions spaced along a total length of  $L = 17.1$  mm. (a) Coupling strength as a function of position  $z$ . The resulting modulation response is shown in (b).

**Funding.** National Natural Science Foundation of China (62204149, 62205193, U23A20356); Natural Science Foundation of Shanghai Municipality (23ZR1442400).

**Acknowledgment.** This work was supported by the Shanghai Collaborative Innovation Center of Intelligent Sensing Chip Technology, and Shanghai Key Laboratory of Chips and Systems for Intelligent Connected Vehicle.

**Disclosures.** The authors declare no conflicts of interest.

**Data Availability.** Data underlying the results presented in this paper are not publicly available at this time but may be obtained from the authors upon reasonable request.

## REFERENCES

- A. H. Safavi-Naeini, D. V. Thourhout, R. Baets, *et al.*, "Controlling phonons and photons at the wavelength scale: integrated photonics meets integrated phononics," *Optica* **6**, 213–232 (2019).
- E. A. Kittlaus, W. M. Jones, P. T. Rakich, *et al.*, "Electrically driven acousto-optics and broadband non-reciprocity in silicon photonics," *Nat. Photonics* **15**, 43–52 (2021).
- M. Bass and Optical Society of America, eds., *Handbook of Optics*, 2nd ed. (McGraw-Hill, 1995).
- C. Huang, H. Shi, L. Yu, *et al.*, "Acousto-optic modulation in silicon waveguides based on piezoelectric aluminum scandium nitride film," *Adv. Opt. Mater.* **10**, 2102334 (2022).
- C. J. Sarabalis, R. V. Laer, R. N. Patel, *et al.*, "Acousto-optic modulation of a wavelength-scale waveguide," *Optica* **8**, 477–483 (2021).
- Z. Yu and X. Sun, "Gigahertz acousto-optic modulation and frequency shifting on etchless lithium niobate integrated platform," *ACS Photon.* **8**, 798–803 (2021).
- L. Shao, N. Sinclair, J. Leatham, *et al.*, "Integrated microwave acousto-optic frequency shifter on thin-film lithium niobate," *Opt. Express* **28**, 23728–23738 (2020).
- D. B. Sohn and G. Bahl, "Direction reconfigurable nonreciprocal acousto-optic modulator on chip," *APL Photon.* **4**, 126103 (2019).
- D. B. Sohn, O. E. Örsel, and G. Bahl, "Electrically driven optical isolation through phonon-mediated photonic Autler–Townes splitting," *Nat. Photonics* **15**, 822–827 (2021).
- H. Shi, C. Huang, L. Yu, *et al.*, "Intramodal acousto-optic scattering of opto-piezomechanical device on aluminum nitride," *J. Lightwave Technol.* **41**, 6348–6355 (2023).
- H. Tian, J. Liu, A. Siddharth, *et al.*, "Magnetic-free silicon nitride integrated optical isolator," *Nat. Photonics* **15**, 828–836 (2021).
- E. A. Kittlaus, N. T. Otterstrom, P. Kharel, *et al.*, "Non-reciprocal interband Brillouin modulation," *Nat. Photonics* **12**, 613–619 (2018).
- Y. Schrödel, C. Hartmann, J. Zheng, *et al.*, "Acousto-optic modulation of gigawatt-scale laser pulses in ambient air," *Nat. Photonics* **18**, 54–59 (2023).
- G. Pillai and S.-S. Li, "Controllable multichannel acousto-optic modulator and frequency synthesizer enabled by nonlinear MEMS resonator," *Sci. Rep.* **11**, 10898 (2021).
- B. Li, Q. Lin, and M. Li, "Frequency-angular resolving LiDAR using chip-scale acousto-optic beam steering," *Nature* **620**, 316–322 (2023).
- I.-T. Chen, B. Li, S. Lee, *et al.*, "Optomechanical ring resonator for efficient microwave-optical frequency conversion," *Nat. Commun.* **14**, 7594 (2023).
- S. A. Tadesse and M. Li, "Sub-optical wavelength acoustic wave modulation of integrated photonic resonators at microwave frequencies," *Nat. Commun.* **5**, 5402 (2014).
- L. Shao, M. Yu, S. Maity, *et al.*, "Microwave-to-optical conversion using lithium niobate thin-film acoustic resonators," *Optica* **6**, 1498–1505 (2019).
- Y. Yu and X. Sun, "Surface acoustic microwave photonic filters on etchless lithium niobate integrated platform," in *CLEO* (Optica Publishing Group, 2023), paper SW3L.3.
- N. Savage, "Acousto-optic devices," *Nat. Photonics* **4**, 728–729 (2010).
- L. Wan, Z. Yang, W. Zhou, *et al.*, "Highly efficient acousto-optic modulation using nonsuspended thin-film lithium niobate-chalcogenide hybrid waveguides," *Light Sci. Appl.* **11**, 145 (2022).
- J. Liu, G. Huang, R. N. Wang, *et al.*, "High-yield, wafer-scale fabrication of ultralow-loss, dispersion-engineered silicon nitride photonic circuits," *Nat. Commun.* **12**, 2236 (2021).
- C. Xiang, J. Liu, J. Guo, *et al.*, "Laser soliton microcombs heterogeneously integrated on silicon," *Science* **373**, 99–103 (2021).
- H. Tian, J. Liu, B. Dong, *et al.*, "Hybrid integrated photonics using bulk acoustic resonators," *Nat. Commun.* **11**, 3073 (2020).
- Z. Yang, M. Wen, L. Wan, *et al.*, "Efficient acousto-optic modulation using a microring resonator on a thin-film lithium niobate-chalcogenide hybrid platform," *Opt. Lett.* **47**, 3808–3811 (2022).
- I. Ansari, J. P. George, G. F. Feutmba, *et al.*, "Light modulation in silicon photonics by PZT actuated acoustic waves," *ACS Photon.* **9**, 1944–1953 (2022).
- M. M. De Lima, M. Beck, R. Hey, *et al.*, "Compact Mach-Zehnder acousto-optic modulator," *Appl. Phys. Lett.* **89**, 121104 (2006).
- I. M. Sopko, D. O. Ignatyeva, G. A. Knyazev, *et al.*, "Efficient acousto-optical light modulation at the mid-infrared spectral range by planar semiconductor structures supporting guided modes," *Phys. Rev. Appl.* **13**, 034076 (2020).
- W. Fu, Z. Shen, Y. Xu, *et al.*, "Phononic integrated circuitry and spin-orbit interaction of phonons," *Nat. Commun.* **10**, 2743 (2019).
- L. Cai, A. Mahmoud, M. Khan, *et al.*, "Acousto-optical modulation of thin film lithium niobate waveguide devices," *Photon. Res.* **7**, 1003–1013 (2019).
- S. Kim, D. B. Sohn, C. W. Peterson, *et al.*, "On-chip optical non-reciprocity through a synthetic Hall effect for photons," *APL Photon.* **6**, 011301 (2021).
- R. Matloub, M. Hadad, A. Mazzalai, *et al.*, "Piezoelectric Al<sub>1-x</sub>Sc<sub>x</sub>N thin films: a semiconductor compatible solution for mechanical energy harvesting and sensors," *Appl. Phys. Lett.* **102**, 152903 (2013).
- K.-H. Kim, S. Oh, M. M. A. Fiagbenu, *et al.*, "Scalable CMOS back-end-of-line-compatible AlScN/two-dimensional channel ferroelectric field-effect transistors," *Nat. Nanotechnol.* **18**, 1044–1050 (2023).
- M. Akiyama, T. Kamohara, K. Kano, *et al.*, "Enhancement of piezoelectric response in scandium aluminum nitride alloy thin films prepared by dual reactive cosputtering," *Adv. Mater.* **21**, 593–596 (2009).
- Q. Wang, Y. Lu, S. Mishin, *et al.*, "Design, fabrication, and characterization of scandium aluminum nitride-based piezoelectric micromachined ultrasonic transducers," *J. Microelectromechanical Syst.* **26**, 1132–1139 (2017).
- M. A. Caro, S. Zhang, T. Riekkinen, *et al.*, "Piezoelectric coefficients and spontaneous polarization of ScAlN," *J. Phys. Condens. Matter* **27**, 245901 (2015).
- S. Saada, S. Lakel, and K. Almi, "Optical, electronic and elastic properties of ScAlN alloys in WZ and ZB phases: prospective material for optoelectronics and solar cell applications," *Superlattices Microstruct.* **109**, 915–926 (2017).
- M. Baeumler, Y. Lu, N. Kurz, *et al.*, "Optical constants and band gap of wurtzite Al<sub>1-x</sub>Sc<sub>x</sub>N/Al<sub>2</sub>O<sub>3</sub> prepared by magnetron sputter epitaxy for scandium concentrations up to  $x = 0.41$ ," *J. Appl. Phys.* **126**, 045715 (2019).
- H. Ichihashi, T. Yanagitani, M. Suzuki, *et al.*, "Acoustic-wave velocities and refractive indices in an m-plane GaN single-crystal plate and c-axis-oriented ScAlN films measured by Brillouin scattering techniques," *IEEE Trans. Ultrason. Ferroelectr. Freq. Control* **63**, 717–725 (2016).
- S. Zhu, Q. Zhong, N. Li, *et al.*, "Integrated ScAlN photonic circuits on silicon substrate," in *Conference on Lasers and Electro-Optics (CLEO)* (Optica Publishing Group, 2020), paper STu3P.5.
- K. Bian, Z. Li, X. Zhao, *et al.*, "Integrated scandium-doped aluminum nitride microring resonators on 8-inch silicon wafers," in *Asia Communications and Photonics Conference/2023 International*

- Photonics and Optoelectronics Meetings (ACP/POEM)* (IEEE, 2023), pp. 1–5.
42. Y. Zang, L. Li, Z. Ren, *et al.*, “Characterization of AlN thin film prepared by reactive sputtering,” *Surf. Interface Anal.* **48**, 1029–1032 (2016).
  43. D. B. Sohn, S. Kim, and G. Bahl, “Time-reversal symmetry breaking with acoustic pumping of nanophotonic circuits,” *Nat. Photonics* **12**, 91–97 (2018).
  44. D. Dai and S. Wang, “Asymmetric directional couplers based on silicon nanophotonic waveguides and applications,” *Front. Optoelectron.* **9**, 450–465 (2016).
  45. E. A. Kittlaus, N. T. Otterstrom, and P. T. Rakich, “On-chip inter-modal Brillouin scattering,” *Nat. Commun.* **8**, 15819 (2017).
  46. O. Jafari, S. Zhalehpour, W. Shi, *et al.*, “Mode-conversion-based silicon photonic modulator loaded by a combination of lateral and interleaved p-n junctions,” *Photon. Res.* **9**, 471–476 (2021).
  47. C. Huang, H. Shi, L. Yu, *et al.*, “Piezoelectrically coupling surface acoustic waves to silicon waveguides,” *Opt. Open Prepr.* (2023).
  48. Q. Liu, H. Li, and M. Li, “Electromechanical Brillouin scattering in integrated optomechanical waveguides,” *Optica* **6**, 778–785 (2019).
  49. M. Uehara, T. Mizuno, Y. Aida, *et al.*, “Increase in the piezoelectric response of scandium-doped gallium nitride thin films sputtered using a metal interlayer for piezo MEMS,” *Appl. Phys. Lett.* **114**, 012902 (2019).
  50. L. Zhang, C. Cui, P.-K. Chen, *et al.*, “Integrated-waveguide-based acousto-optic modulation with complete optical conversion,” *Optica* **11**, 184–189 (2024).
  51. R. T. Smith and F. S. Welsh, “Temperature dependence of the elastic, piezoelectric, and dielectric constants of lithium tantalate and lithium niobate,” *J. Appl. Phys.* **42**, 2219–2230 (1971).
  52. E. Österlund, G. Ross, M. A. Caro, *et al.*, “Stability and residual stresses of sputtered Wurtzite AlScN thin films,” *Phys. Rev. Mater.* **5**, 035001 (2021).
  53. Z. Luo, S. Shao, and T. Wu, “Characterization of AlN and AlScN film ICP etching for micro/nano fabrication,” *Microelectron. Eng.* **242–243**, 111530 (2021).
  54. D. Royer and E. Dieulesaint, *Elastic Waves in Solids II: Generation, Acousto-Optic Interaction, Applications* (Springer, 1999).
  55. J. H. Hines and D. C. Malocha, “A simple transducer equivalent circuit parameter extraction technique,” in *1993 Proceedings IEEE Ultrasonics Symposium* (IEEE, 1993), Vol. 1, pp. 173–177.